Carbon 229 (2024) 119506

Contents lists available at ScienceDirect

Carbon

journal homepage: www.elsevier.com/locate/carbon

Research paper

Atomistic-to-continuum modeling of carbon foam: A new approach to finite element simulation

C. Ugwumadu [a,*], W. Downs [b], C. O'Brien [b], R. Thapa [c], R. Olson III [d], B. Wisner [b], M. Ali [b], J. Trembly [b,e], Y. Al-Majali [b,e], D.A. Drabold [a]

[a] Department of Physics and Astronomy, Nanoscale and Quantum Phenomena Institute (NQPI), Ohio University, Athens, 45701, OH, USA
[b] Department of Mechanical Engineering, Ohio University, Athens, 45701, OH, USA
[c] Department of Material Science and Engineering, Institute for Functional Materials and Devices, Lehigh University, Bethlehem, 18015, PA, USA
[d] CONSOL Innovations LLC, Triadelphia, 26059, WV, USA
[e] Institute for Sustainable Energy and the Environment (ISEE), Ohio University, Athens, 45701, OH, USA

ARTICLE INFO

Dataset link: 10.5281/zenodo.10809805, https://people.ohio.edu/drabold/carbonfoam/

Keywords:
Carbon foam
Porous media
Fractal dimension
Molecular dynamics simulation
Finite element analysis

ABSTRACT

Carbon foam materials exhibit useful characteristics for unique and diverse applications. However, accurately modeling three-dimensional carbon foam remains a significant challenge. This paper introduces a novel technique for transitioning atomistic-scale models of porous carbon, obtained via molecular dynamics simulation, to continuum-scale carbon foam models suited for finite element simulations. We present our method using the fractal properties of porous media, specifically carbon foams. The resulting models demonstrate testable properties consistent with those derived from computed tomography (CT) scans and experimental data. Stress–strain curves obtained from finite element analysis (FEA) calculations of our models correlate well with experimental measurements from dogbone testing samples of carbon foam sourced from CONSOL Innovations LLC, WV, USA, as well as CT scan models derived from the carbon foams. Our approach presents a computationally efficient alternative and encourages innovation in modeling porous media, particularly in extracting physical properties from an ensemble of models.

1. Introduction

Carbon foams are porous structures rendering appealing for diverse engineering applications, as their thermal, electrical, and mechanical attributes can be tailored by adjusting manufacturing parameters [1,2]. However, the inherently stochastic pore geometry poses challenges in analyzing the material's properties and behavior for applications [3,4]. Finite Element Analysis (FEA) is a continuum-scale simulation method (refer to Fig. 1) that aids in the study of the engineering (macroscopic) properties of materials. FEA is a computational technique to predict how materials respond to vibration, heat, fluid flow, and other physical phenomena. Predicting and understanding the properties of carbon foams hinges on the availability of computer models that offer realistic descriptions of the material useful for FEA.

Earlier research on carbon foams has often relied on simplified geometries with periodically distributed pores to approximate its microstructure [5–8]. However, these models frequently fall short of accurately predicting foam properties and performance in practical engineering contexts due to their failure to account for the distribution of pore sizes and the role of rare features that may determine properties like brittle tensile response. Efforts have been made to address this randomness in pore distribution. One method employs Voronoi tessellation to study carbon foam properties [9–11]. Another approach utilizes computer-aided design (CAD) to construct computer models of carbon foam with varying pore distributions, achieved by manipulating spherical geometries and their intersections to form "bubbles" and pores [12,13]. Additionally, Yue et al. constructed 3-D micro-structure models based on the nucleation and growth process of pores to match certain geometrical features of an actual carbon foam [14].

In recent years, CT (Computed Tomography) scanning has emerged as a promising technique for constructing models of foam materials useful for finite element simulations [15–17]. CT scanning offers numerous advantages, including nondestructive and non-invasive imaging; this is necessary for preserving the intricate pore network that is essential for mechanical and thermal analysis. Furthermore, it produces 2D images to facilitate 3D reconstruction of the foam's microstructure. The digital nature of CT data also simplifies manipulation and conversion into finite element meshes for further analysis. However, CT scanning has

* Corresponding author.
E-mail addresses: cu884120@ohio.edu (C. Ugwumadu), wd620322@ohio.edu (W. Downs), drabold@ohio.edu (D.A. Drabold).

https://doi.org/10.1016/j.carbon.2024.119506
Received 7 June 2024; Received in revised form 23 July 2024; Accepted 29 July 2024
Available online 2 August 2024

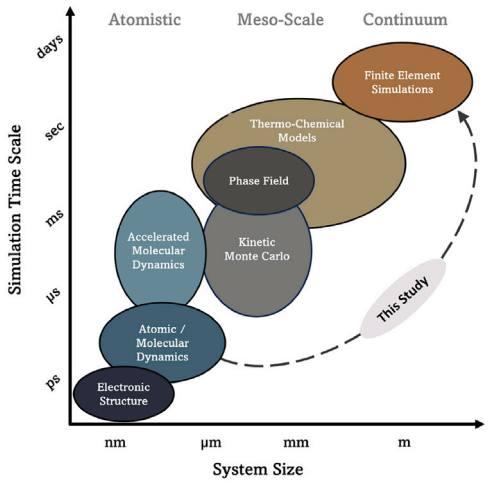

Fig. 1. Schematic illustration of the simulation time scale and the corresponding system size across different computer simulation techniques. The arrow signifies the goal of this study: transitioning atomistic to continuum models suitable for finite element analysis.

limitations. The limited resolution of CT scans may overlook small-scale features, like micro- and mesopores, within the foam structure. Interpreting CT images requires addressing image artifacts and noise, which can impact model accuracy. Finally, analyzing large CT datasets and generating finite element meshes demand significant computational resources and processing time, especially for complex foam geometries.

Acknowledging these limitations, this study proposes an alternative approach. By leveraging atomistic models of porous carbon constructed from molecular dynamics (MD) simulation [18], a framework is devised to transition from the atomistic-scale models to continuum-scale models suitable for finite element simulations. Fig. 1 illustrates the disparate time scales of computer simulation techniques and their corresponding system sizes, with the arrow indicating the objective of this study. A substantial body of research has been focused on transitioning from atomic to continuum models [19–23], and the invention of high-resolution imaging techniques also serves to bridge the gap in research between the computational scales [24,25]. The vast range of length scales displayed in Fig. 1, prompts a fundamental question: *Can atomistic-scale structures be employed for finite element simulation?* Porous media, such as carbon foams, exhibit statistical self-similarity which constitutes a characteristic trait of fractal geometries [26–31]. Thus, we show that it becomes possible to extrapolate nanoscale to macroscale structures in diverse circumstances. We elucidate this with mathematical analysis and compare it to experiments.

We summarize our approach as follows: (1) We describe a pathway for investigating nano-scale properties derived from chemically and structurally realistic atomic porous carbon models alongside macroscopic properties derived from associated continuum models of carbon foams. (2) The computational overhead associated with MD simulation-derived models is notably lower compared to representative volume elements (RVE) obtained via CT scan while offering a more comprehensive portrayal of porosity and pore distribution than idealized or mathematically derived carbon foam models. (3) The seamless construction of these models enables the generation of a large ensemble with diverse structures, ensuring statistical accuracy in the analysis of carbon foam properties.

2. Methods

2.1. The Gaussian approximation potential for carbon

As depicted in Fig. 1, the constraints of molecular dynamics simulations become apparent when striving for the precision of density functional theory (DFT) calculations [32]. These constraints derive from the system size and the simulation time scale [33]. Recent advances in machine learning applications have paved the way for the development of novel inter-atomic potentials capable of simulating thousands [34–36], if not millions [37,38], of atoms. Among these potentials, the Gaussian Approximation Potential (GAP) stands out and is utilized in this study [39]. The GAP potential for carbon interactions is trained using the conventional approach, involving fitting to an extensive dataset derived from DFT simulations [40–44]. For this work, it was implemented within the "Large-scale Atomic/Molecular Massively Parallel Simulator" (LAMMPS) software package [45]. We note that GAP has proven effective in the exploration of amorphous phases across various carbon allotropes, including amorphous graphite [46, 47], multi-shell fullerenes [48], and multi-wall carbon nanotubes [49].

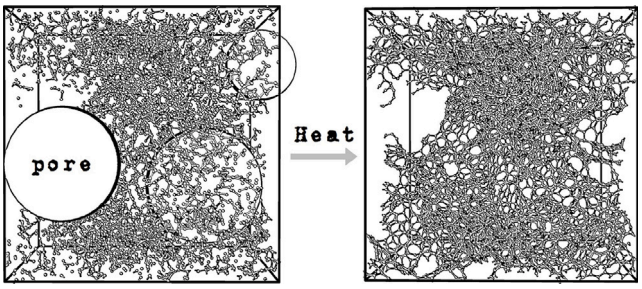

Fig. 2. Construction of the porous carbon models. [LEFT] The initial configuration with artificial pores distribution. [RIGHT] The final configuration after heating in NVT ensemble and energy optimization. The atoms are free to occupy some regions in the initial pore volume to achieve an optimized configuration.

2.2. Protocol for constructing atomistic models

The method for constructing porous carbon has been detailed in Ref. [18]. However, for completeness, the methodology is recapped here, with some variations. Initially, carbon atoms and spherical void regions are randomly distributed in a cubic box at a chosen density, as depicted in Fig. 2 [LEFT]. Pore radii are sampled from a uniform, chi, or beta distribution, extending maximally to half the bounding box length (L) to prevent finite-size artifacts. The system density is set by specifying the system size, bounding box volume, and porosity. For convenience to the interested reader, we built a Web App, *Porous Carbon Constructor*, that generates initial porous carbon models which can then be used for MD simulation. The URL to the Web App, deployed on Streamlit [50], is provided in Ref. [51], and the open-source code is available on GitHub (accessible via the app). The procedure for obtaining the porous carbon model is outlined below:

1. Determine the desired initial porosity (ξ_i) using the equation below [18]:

$$\xi_i = \sum_{n=1}^{N} \frac{v_n}{V} \tag{1}$$

   where N, v_n, and V are the total number of pores, the pore volume sampled from a uniform, chi or beta distribution, and the bounding box volume, respectively.
2. Select the pore centers if pore overlaps are to be avoided. This aims to maintain the initial porosity.
3. Randomly distribute carbon atoms in the simulation box, ensuring they do not fall inside the pore volume. Apply periodic boundary conditions [52] throughout this process.
4. Perform molecular dynamics (MD) simulation using GAP to obtain optimal porous carbon configuration (see example in Fig. 2 [RIGHT]).

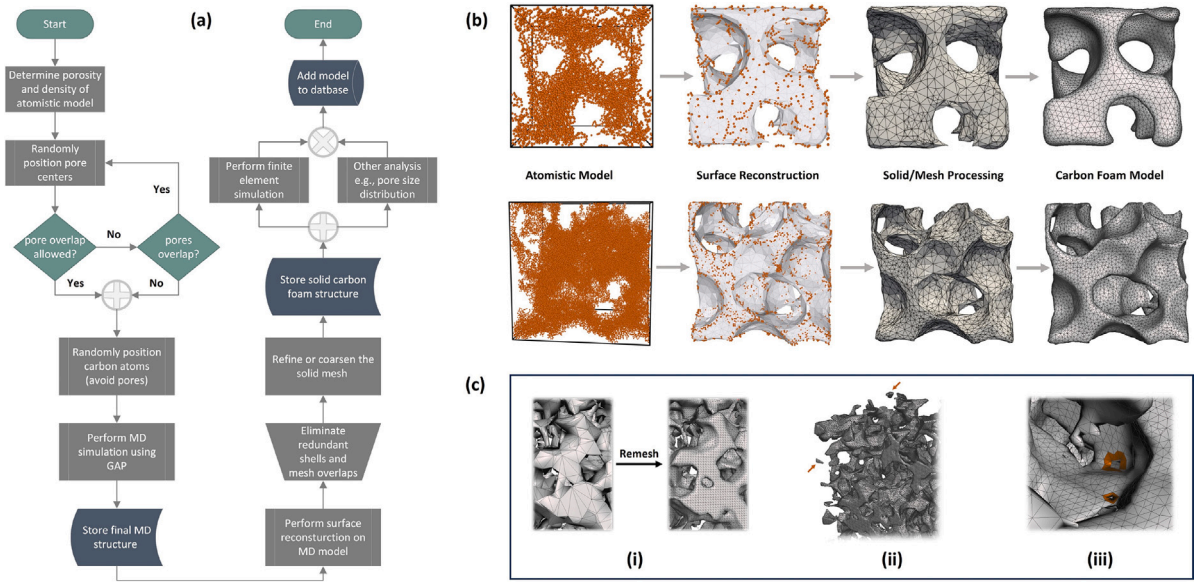

Fig. 3. (a) Flowchart of the protocol to construct macroscopic (solid) carbon from models starting from atomistic model construction; (b) a depiction of the various stages. (c) Common problematic features observed during the surface reconstructed atomistic models. These features include (i) poor surface mesh (left) and outcome after mesh refinement (right), (ii) isolated shells or volumes (indicated by the brown arrows), and (iii) open surfaces (holes) in solid carbon foam models. The region around the holes is shaded in brown. (For interpretation of the references to color in this figure legend, the reader is referred to the web version of this article.)

5. Construct surface manifold (with vertices and faces) from the 3D morphology of the connected carbon network utilizing the alpha-shape method [53] on a constructed Delaunay tessellation [49,54,55]. This generates a geometric mesh describing the interior and exterior spatial boundaries of the atomistic structure.

In *Step 4*, the MD simulation to construct the models, using GAP, was conducted under fixed conditions of particle number (N), volume (V), and temperature (T), representing canonical (NVT) thermodynamic conditions. A timestep of 1 fs was applied to update atomic positions and velocities. The Nosé–Hoover thermostat [56,57] was utilized in rescaling the temperature every 100 fs (100 timesteps). Initially, the starting models were equilibrated at 550 K for 50 ps. The temperature was then increased to 1500 K over 100 ps and maintained at this temperature for 60 ps, allowing the atoms to adequately sample the configuration space and initiate crosslinking of carbon atoms without graphitization [18,46]. The temperature was then reduced to 1000 K, close to foaming temperature [58], over 100 ps and equilibrated for another 120 ps to ensure convergence of the total system energy. Finally, the system was cooled to 300 K over 70 ps and relaxed to an energy-optimal configuration using the conjugate gradient method in `LAMMPS`.

For surface reconstruction in *step 5*, a probe sphere radius (R_α) of 3 Å was set for the alpha-shape method in `OVITO` [59], and a maximum of 30 iterations of the smoothing and fairing procedure [60] was applied to remove atomically sharp surface steps. The final surface manifolds were saved in VTK (Visualization Toolkit) file format [61]. Although alternative 3D graphics or volume rendering file systems can be employed, VTK is recommended owing to its adaptability and facile conversion to Stereolithography (STL) file format [62], which is imperative for representing 3D surfaces in triangular facets.

2.3. Protocol for constructing FEA models

A flowchart for constructing carbon foam models for FEA, originating from atomistic porous carbon models, is delineated in Fig. 3a. Beginning with the relaxed atomistic porous carbon network, solid models are derived through surface reconstruction, solid body preprocessing, and solid mesh refinement, as depicted in Fig. 3b. Hereafter, the FEA models constructed from atomistic molecular dynamics simulation will be referred to as the *MD models*. Subsequent discussions will focus on three carbon foam MD models. As shown in Table 1, The first model, *MD1*, has 64,000 atoms, and the other two models, *MD2* and *MD3*, both have 10,000 atoms each. The models' initial porosities (ξ_i) were set at 70%, for MD1 and MD2, and at 80% for MD3. The MD models are shown in the top panel of Fig. 4 and the structure files (in STL format) of the MD models are provided as supplementary material, and on our website [63].

Some challenging aspects commonly encountered in the construction of MD models are illustrated in Fig. 3c. These include: (3c-i) Inadequate surface mesh quality, as depicted in the left figure, and the subsequently improved outcome after mesh refinement shown in the right figure; (3c-ii) Presence of disjointed or isolated shells or volumes (indicated by brown arrows) in the STL file, which are artifacts of the surface reconstruction of the atomistic model; (3c-iii) Occurrence of open surfaces (holes) within solid carbon foam models, visually highlighted by a brown shading around the affected regions. Below, we discuss solutions to address these issues, alongside the procedure to build the MD models:

1. Convert the initial VTK file of the surface reconstructed atomistic model into STL file format. This step facilitates mesh refinement of the solid and can be accomplished using the `Paraview` software package [64,65].
2. Delete isolated shells in poorly connected regions in the network and remove disconnected mesh regions. This is done using the Autodesk® `Meshmixer` software package and aims to resolve surface mesh overlap.
3. Optimize the solid mesh by refining or coarsening it according to the specific area of interest and by varying loading conditions. Adaptive meshing enhances computational efficiency by adjusting mesh size, allocating fewer resources to areas of lesser interest or anticipated lower complexity in loading scenarios.
4. Address any open surfaces or holes by filling them and by refining the mesh in the affected areas (if necessary). Note that repairing the holes may remove geometry from the model.
5. To ensure the adequacy of mesh quality for FEA, the following criteria should be satisfied:

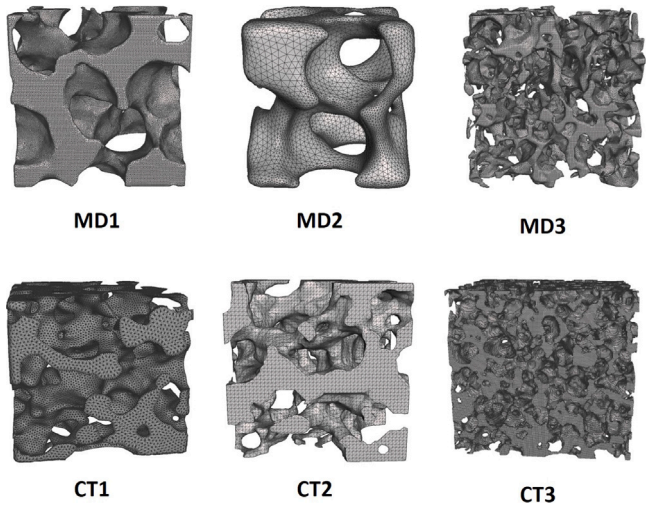

Fig. 4. [Top] The MD models, MD1, MD2, and MD3. [Bottom] The CT models, CT1, CT2, and CT3, derived from the CFOAM® carbon foam material.

(a) The aspect ratio of each mesh, defined as the ratio of the longest side to the shortest, must be less than 10.
(b) The mesh dihedral angles must fall within the range of 30° to 150° to ensure adequate element volume and mitigate element "flatness".

6. Upload the final solid model to any FEA software, such as Abaqus® (used in this study), for testing, validation, and characterization.

2.4. Tensile properties

To validate the MD models, we computed their tensile properties and compared the results with experimental tensile data obtained from a carbon foam material. The carbon foam material used in this study is a coal-derived carbon foam, CFOAM®, sourced from CONSOL Innovations LLC (WV, USA). Additionally, we constructed carbon foam models from 3D reconstructions of CT scanning of the CFOAM® material, henceforth referred to as *CT models*. Although five CT models were constructed and included as supplementary material, we focus on discussing only three: CT1, CT2, and CT3 for consistency with the MD models. These models are depicted in the lower panel of Fig. 4. Collectively, the MD and CT models will be referred to as *FEA models*.

The CT models were generated in Amira-3D software utilizing these modules (in the order): *Extract Subvolume → Auto Thresholding → Generate Surface → Scan Surface to Volume → Compute Volume Fraction → Generate Tetrahedral Mesh*. The criteria for an acceptable mesh are outlined in *step 5* of the description on how to build MD models (Section 2.3). This methodology in Amira-3D was employed exclusively for processing the CT scan data.

2.4.1. Experiment

Fifteen CFOAM® dogbone samples were cut from sheets using a ProtoMAX waterjet and designed to a uniform thickness with the NANO 1000T Grinder/Polisher from Pace Technologies. Tensile tests were conducted using a 1.6 kN Psylotech Micro-testing (μTs) device. The samples were subjected to uniaxial tension until failure under a monotonic increasing load at 2.5 μm/s (0.15 mm/min), with data acquisition at a sampling rate of 20 Hz. To minimize surface effects on the grip section, the samples were further sanded with 600-grit sandpaper. A Linear Variable Differential Transformer (LVDT) [66], attached to and positioned near the crosshead of the Psylotech testing device, was used for strain measurement.

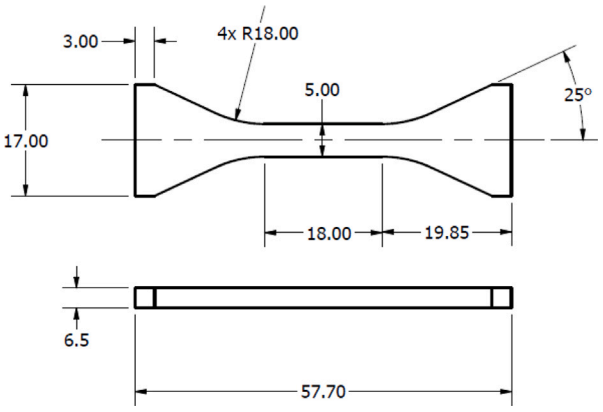

Fig. 5. A schematic illustration of the geometry (in mm) of the CFOAM® dogbone samples used for tensile testing. The cross-sectional area (A_e) for the dogbone is 6.5 × 5 mm^2.

In the absence of an ASTM standard for monotonic tensile testing of brittle carbon foam, the sample geometry (dogbone) for the tensile tests was designed to meet the specifications of the Psylotech device [69], as illustrated in Fig. 5. The 25° grip region was optimized to enhance the tension grip feature of the Psylotech device. To ensure the bulk response of the carbon foam, we increased the recommended sample thickness from 3 mm to 6.5 mm. This adjustment was made because a thinner gauge section does not sufficiently represent the foam structure in tension, as it does not include enough struts.

2.4.2. Finite element simulation

Finite element simulations were conducted on a VRLA Tech workstation with an AMD Ryzen Threadripper 5965WX 3.8 GHz 24-Core CPU, 256 GB DDR4 3200 MHz ECC RAM, and an Nvidia RTX4090 24 GB GPU.

The elastic and plastic properties for the FEA models were computed using the standard and explicit solvers in Abaqus®, respectively. Experimental parameters for carbon foam were used as input to compute the FEA tensile properties. These parameters, presented in the lower section of Table 1, include the elastic modulus, strength, strain to failure (obtained from our experiment) and Poisson's ratio (sourced from literature [67,68]).

To validate the solid model on experimental data, we employed the single-element-model method (typically described in introductory FEA textbooks) to determine the hydrostatic cutoff stress. Specifically, we utilized the hexahedral C3D8 element type, and based on experimental strain-to-failure of 1.157%, a strength value of 5.88 MPa was obtained from the model (see Table 1).

Given the phenomenological nature of finite element methods, the parameters used in finite element simulations are dependent on experimental data [70]. For the tensile simulation, a scaling factor (ζ) is required to relate the experimental forces to the input for FEA. The governing equation becomes:

$$\zeta \propto \frac{F_e}{F_m} = \frac{A_e}{A_m}\rho_r \tag{2}$$

where F_e is the average force obtained from experiment (≈20.5 N) and F_m is the force calculated for the FEA models. A_e and A_m are the corresponding cross-sectional areas. The relative density, ρ_r, is defined as:

$$\rho_r = \frac{\rho_e}{\rho_m} \tag{3}$$

where ρ_e and ρ_m denote the density of the dogbone specimen and the FEA model, respectively. Utilizing the defined variables, a uniaxial

Table 1
Derived properties of the MD and CT models[a], and carbon foam parameters used for FEA[b].

	MD1	MD2	MD3	CT1	CT2	CT3
ξ	68.7	71.8	84.2	70.0	70.3	70
λ_{min}	0.284	0.218	0.062	4.312	4.692	23.210
λ_{max}	31.54	17.52	14.67	366.10	361.92	509.31
γ	0.009	0.012	0.004	0.012	0.014	0.046
L	137.0	69.1	67.4	1661.8	1215.3	3685.3
β_{min}	0.002	0.003	0.001	0.003	0.004	0.006
β_{max}	0.230	0.253	0.218	0.220	0.298	0.138
S_2	1.26	1.25	1.41	–	–	–
S_3	2.49	2.42	2.53	2.60	2.47	2.68
D	2.90	2.93	2.97	2.92	2.92	2.88
τ	1.49	1.44	1.62	1.65	1.50	1.50
No. of atoms	64,000	10,000	10,000	–	–	–
No. of Nodes	25,298	20,610	598,277	86,855	60,939	1,598,973
No. of Elements	106,068	78,812	1,818,852	377,153	193,804	7,069,336
Parameters	Modulus	Strength	Poisson's Ratio	Strain-to-Failure		
Values	1022.22 MPa	5.88 MPa	0.33 [67,68]	1.157%		

[a] ξ is the porosity (in %), λ_{min} and λ_{max} is the minimum and maximum pore size (in μm) with and γ taken as the their ratio. L is the average bounding box length (in μm), β_{min} (β_{max}) is the minimum (maximum) pore-to-box ratio. S_2 and S_3 are the 2D and 3D box counting dimensions. D is the pore fractal dimension, and τ is the tortuosity.
[b] Carbon foam properties (parameters) and their respective values.

tension equation for finite element simulation is then obtained as [71]:

$$\sigma(\epsilon) = E\left(1.1\epsilon + 3.74\epsilon^2 + 0.0343\rho_r^{-1}\epsilon^3\right) \tag{4}$$

Here, σ, ϵ, and E denote the stress, strain, and the experimental elastic modulus, respectively, from which a stress–strain relation can be inferred [72].

For the FEA implementation, we maintained uniform initial conditions (i.e. geometrical ratio, boundary, and loading conditions) across all models before adopting any computational or characterization procedures, thus ensuring the credibility of the ensuing results. Consequently, all the models were assigned the same initial elastic and plastic properties using data obtained from experimental testing. Linear tetrahedral elements of type C3D4 were used for the models. The loading regimen for the models is governed by displacement, wherein the top surfaces of the models were equally displaced utilizing the displacement ratio derived from the experiment. The number of nodes and elements for each model are detailed in Table 1.

3. Results & discussion

3.1. Simulation of atomistic models

The manufacturing process of CFOAM® involves subjecting coal to temperatures ranging from 500 to 800 K under a fixed pressure of approximately 500 psi to obtain the *green foam* [58,73]. During this process, volatiles are released, primarily composed of hydrogen, carbon, oxygen, nitrogen, and sulfur, along with areas of the coal becoming molten. Concurrently, carbon atoms undergo cross-linking to generate three-fold coordinated structures reminiscent of sp^2 hybridization found in graphite. These synchronized reactions culminate in the production of the final porous material – the carbon foam [58].

Given the complexity and time constraints associated with molecular dynamics simulation of these intricate reactions (refer to Fig. 1), our approach to simplifying these processes involves initiating pore formation at the outset of the simulation, thus circumventing the need to model the devolatilization stage. Furthermore, we opted to disregard the isobaric component, which primarily pertains to the release of volatiles [73], as they are not integral to the initial configuration of our models. Consequently, our simulation method predicts the dynamics of pore formation and the subsequent cross-linking of the residual carbon atoms to form the three-coordinated conformation in both the bulk and surface regions, mirroring the properties of carbon foam. It is pertinent to note that the fixed volume and atom count in the initial configuration inherently set the density, which is intentionally fixed to align with the experimental density of the final carbon foam (between 0.3 to 1.0 g/cm^3). We included an animation (as supplementary material) that depicts the pore formation and cross-linking of the carbon atom during heating, starting from randomly distributed carbon atoms to form a three-coordinated configuration on the pore surfaces.

3.2. Fractal and pore characteristics of the models

A dramatic assumption of our method to use atomistic models as representative structures of carbon foam for continuum scale simulation hinges on the conjecture that the pore shape and pore size of any porous medium have statistically self-similar fractal geometries [26,28,29]. In this section, we analyze the fractal characteristics of the MD models using the box-counting method. We extend the discussion to include the pore fractal dimension which sets the stage for the applicability and justification of fractal geometry for our atomistic-to-continuum approach.

3.2.1. 2D and 3D box-counting dimensions

Fractal dimension quantifies the complexity and space-filling attributes of patterns or structures, indicating their non-integer scaling behavior across different measurement scales. To assess the fractal properties of the FEA models, we calculated the box-counting (or Minkowski) dimension [74,75] in 2D (for the MD models alone) and in 3D using the equation:

$$\log N(1/\phi) \approx -S_d \log \phi \tag{5}$$

Here, N is the number of boxes of side length ϕ, required to cover the filled region of the carbon foam unit cell, while S_d, the slope, is referred to as the 2D ($d = 2$) or 3D ($d = 3$) box-counting dimension. The log–log plots of N versus ϕ, for the 2D box-counting calculations, are shown in the left panels of Fig. 6a, b, and c for MD1, MD2, and MD3, respectively. The slope of the regression line (black dashed line) indicates the 2D box-counting dimension for MD1 (1.26), MD2 (1.25), and MD3 (1.41). To obtain 2D images for the fractal analysis, the 3D models were sliced into 2D, with each slice having a thickness of 5 μm, as depicted in Fig. 6a (inset). The box-counting method was applied to each slice, as illustrated in Fig. 6b (inset). The 2D box-counting calculation was implemented using the `PoreSpy` toolkit [76].

The viability of the box-counting method for assessing the fractal properties of the MD models was gauged by tracking the convergence of the box-counting dimension across varying box sizes (S versus ϕ). These convergence plots for MD1, MD2, and MD3 are portrayed in the right panels of Fig. 6a, b, and c, respectively. The horizontal regions of the curves indicate the range where the box-counting method remains

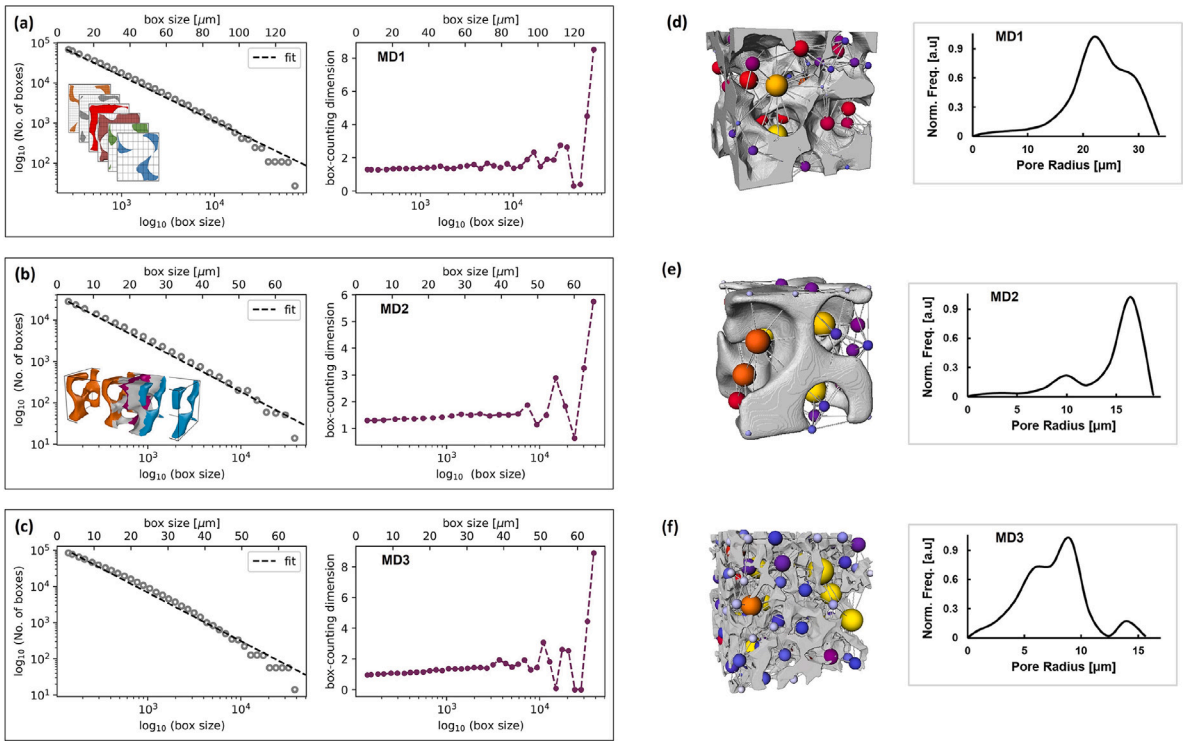

Fig. 6. The box-counting method employed to analyze 2D fractal characteristics of MD models. The left and right plots in a, b, and c represent the Log–log plots of filled boxes versus box sizes, and the convergence of the box-counting dimensions for MD1, MD2, and MD3, respectively. The 3D solid models were sliced into 2D images of varying thicknesses (inset in (a)) for box-counting (inset in (b)). The pore distributions of MD models (d) MD1, (e) MD2, and (f) MD3 are illustrated using spheres to represent pores and color-coded by sizes. The throats of the pore network are depicted as connecting gray wires. Similar representations of the pore distribution of the CT models are shown in Figure S1. (For interpretation of the references to color in this figure legend, the reader is referred to the web version of this article.)

applicable. Beyond this threshold, the finite size of the model begins to influence the analysis, leading to the divergence observed in the plots for larger box sizes. Notably, the box-counting method can be effectively applied to more than half of the bounding box length in MD1, MD2, and MD3, which is 137.0, 69.1, and 67.4 μm, respectively, as detailed in Table 1.

We abstained from computing the 2D box-counting dimensions for the CT models, opting instead to obtain the 3D box-counting dimension for all the models (as detailed in Table 1). The process for computing the 3D box-counting dimension closely resembles that of the 2D method, without the need for slicing; cubes are employed instead of squares for binning to ascertain the count N. Our algorithm for computing the 3D box-counting dimension of the models, facilitated by Wolfram `Mathematica` [77], is provided as supplementary material and available on our website [63].

The mean 3D box-counting dimension for the FEA models is determined to be 2.5317 ± 0.0386. Interestingly, the MD models exhibit a consistent pattern across both 2D and 3D box-counting dimensions, with MD1 and MD2 displaying closer values than MD3. This observation suggests a persistent fractal nature, as anticipated, regardless of system size. However, it also implies the potential influence of porosity and pore distribution on the fractal properties of the carbon foam. Thus, exploring an alternate mode of fractal characterization becomes imperative: the 3D pore fractal dimension of the models.

3.2.2. Pore fractal dimension

Katz and Thompson experimentally showed that the pores in sandstone samples exhibit fractal characteristics with self-similarity across length scales ranging from 10 Å to 100 μm [28]. They established a correlation between porosity (ξ) and the pore fractal dimension (D) of sandstone as:

$$\xi = A\left(\frac{l_1}{l_2}\right)^{3-D} \tag{6}$$

where, A is a constant typically of order one, while l_1 and l_2 denote the lower and upper limits of the self-similar regions, respectively. Theoretically conceived but empirically validated for predicting the fractal dimensions of structures like the porous textile fabric and Serpiǹski carpet and gasket, Yu and Li introduced the unified model for the fractal characterization of porous media [29]:

$$D = d - \frac{\ln \xi}{\ln \gamma} \quad : \quad \gamma \approx \frac{\lambda_{\min}}{\lambda_{\max}} \tag{7}$$

Here, γ represents the *pore ratio*, defined as the ratio between the minimum ($\lambda_{\min}$) and maximum ($\lambda_{\max}$) pore sizes and d (assumed as 2 or 3) signifies two- or three-dimensional space. Notably, Eqs. (6) and (7) are equivalent when $A = 1$, $d = 3$, $l_1 = \lambda_{\min}$, and $l_2 = \lambda_{\max}$. In our examination of the pore fractal dimension for the FEA models using the unified model, we define $\lambda_{\min}$ and $\lambda_{\max}$ as the minimum and maximum pore sizes within the representative volume element [29], as shown in Table 1 for the MD and CT models.

To determine $\lambda_{\min}$ and $\lambda_{\max}$, the pore distributions within the models were computed utilizing the *Pore Network Module* integrated within `Avizo`®. These distributions are presented in the right panel of Fig. 6d, e, and f for MD1, MD2, and MD3, respectively. Corresponding representations for the CT models can be found in Figure S1. In these depictions, the pores within the models are visualized as spheres of different sizes, each color-coded to indicate specific size categories. The interconnecting gray wires represent the throats of the network, facilitating transport between interconnected pores. It is worth noting that, aside from MD3, which has a porosity of 84.2%, the porosities observed for MD1, MD2, and all CT models approximate 70%. It is reiterated that the porosities for the MD models were predetermined during the construction of the models.

Table 1 shows the models' mean pore fractal dimension of 2.92 ± 0.0124. Despite variations in the average length of the bounding box enclosing the FEA models (indicated as L in Table 1), the pore

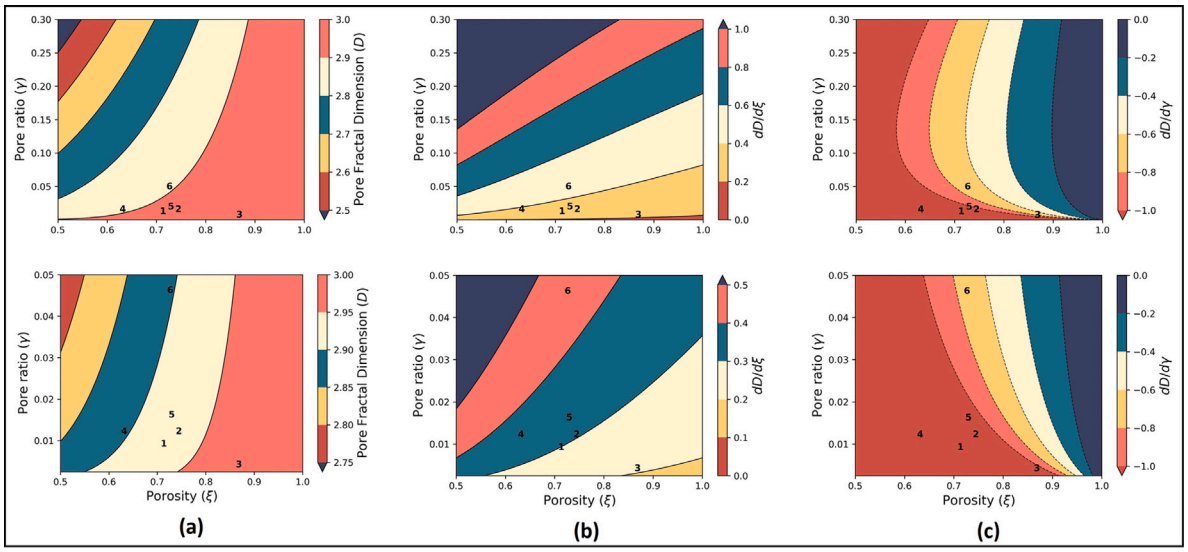

Fig. 7. Contour plots depicting the relationship between porosity, pore ratio, and pore fractal dimension across the models. The lower panel showcases a narrow range of the pore ratio. These plots delineate the characteristics of the models within the pore configuration space (a), with annotations "1" through "6" corresponding to MD1 through CT3 as organized in Table 1. Panels (b) and (c) illustrate the sensitivity of the pore fractal dimension to changes in the pore ratio and porosity, respectively. Full and dashed lines denote positive and negative contours, respectively, while the color bar signifies regions within a specified range. (For interpretation of the references to color in this figure legend, the reader is referred to the web version of this article.)

fractal dimensions remain closely matched. This observation suggests a fundamental statistical self-similarity within the structure of the carbon foam – a concept pivotal for validating the atomistic-to-continuum approach implemented in this study and discussed in the subsequent section.

To further elucidate the nature of pore fractals in the models, we introduce a parameter, the *pore-to-box* ratio, denoted as β_{m}, where:

$$\beta_{\mathrm{m}} = \frac{\lambda_{\mathrm{m}}}{L} \tag{8}$$

Here, m represents the minimum or maximum pore size. Although individual values of the parameters in Eq. (8) exhibit considerable variability across models, β_{min} and β_{max} closely match for all models, as outlined in Table 1. Furthermore, the interrelationship among the pore ratio (γ), porosity (ξ), and pore fractal dimension (D) in Eq. (7) is visually depicted using color-filled contour lines in Fig. 7a. The plot in the upper panel of Fig. 7a shows that the pore fractal dimension varies smoothly with the porosity and sharply with the pore ratio. The first-order derivative of Eq. (7) with respect to ξ (Fig. 7b), while maintaining γ constant, and vice versa (Fig. 7c), both illustrates the sensitivity of the pore fractal dimension to small changes in ξ and γ. The consistency in values for the 2D box-counting dimensions of the MD models, the 3D pore fractal dimension, and the pore-to-box ratios of MD models and the CT models, provides evidence for statistical self-similarity and the fractal nature of the MD models [27]. This observation strengthens the validity of the atomistic-to-continuum carbon foam modeling approach discussed in Section 3.2.3 and employed in this study.

We note that the advantage of using the MD model over CT models for FEA is readily apparent upon examination of the significantly reduced node and element counts necessary for finite element calculations, as illustrated in Table 1. In contrast to CT models, MD models, even with dense meshing, require only approximately one-third of the nodes and elements. This reduction is attributed to the MD models' capability to employ smaller RVEs than CT models. Consequently, the computational costs associated with utilizing the MD model are substantially lower than those of the CT model, with virtually no compromise in accuracy.

3.2.3. Analysis of the atomistic-to-continuum transition

We defer the detailed discussion on fractal theory in porous materials to the works presented in Refs. [29,31]. Here, we summarize the argument of Yu and Li [29] on the criterion for characterizing properties of porous media by fractal theory, which has been implemented for carbon foams [31].

Majumdar and Bhushan derived the power law relation [78]:

$$M(A \geq a) = \left(\frac{a_{\mathrm{max}}}{a}\right)^{D_f/2} \tag{9}$$

that accounts for the total number of contact spots (M) on a surface of area, A, greater than a given value, a, given the fractal dimension of the surface, D_f [79]. Subsequently, Yu and Li formulated a similar equation for the cumulative number of pores (N) within porous media [29]:

$$N(l \geq \lambda) = \left(\frac{\lambda_{\mathrm{max}}}{\lambda}\right)^{D} \quad : \quad 0 < D < d \tag{10}$$

Here l and λ denote the length scale and pore size of the porous medium, respectively. Other variables retain their existing definitions (see Eq. (7)). From Eq. (10), the total number of pores, N_{t}, from the minimum to maximum pore size can be calculated as:

$$N_{\mathrm{t}}(l \geq \lambda_{min}) = \left(\frac{\lambda_{\mathrm{max}}}{\lambda_{\mathrm{min}}}\right)^{D} \tag{11}$$

Taking the pore distribution to be a continuous and differentiable function, one can obtain an equation for an infinitesimal change in λ:

$$-\frac{dN}{d\lambda} = D\frac{\lambda_{\mathrm{max}}^{D}}{\lambda^{(D+1)}} \tag{12}$$

Dividing Eq. (12) by Eq. (11) leads to:

$$-\frac{dN}{N_{\mathrm{t}}} = D\frac{\lambda_{\mathrm{min}}^{D}}{\lambda^{(D+1)}}\, d\lambda = f(\lambda)\, d\lambda \tag{13}$$

$f(\lambda)$ can be taken as a probability density function for pores in the porous medium, as such, the normalization condition requires that:

$$\int_{-\infty}^{+\infty} f(\lambda) d\lambda = \int_{\lambda_{\mathrm{min}}}^{\lambda_{\mathrm{max}}} f(\lambda) d\lambda = 1 - \left(\frac{\lambda_{\mathrm{min}}}{\lambda_{\mathrm{max}}}\right)^{D} \tag{14}$$

$$\equiv 1 \iff \left(\frac{\lambda_{\mathrm{min}}}{\lambda_{\mathrm{max}}}\right)^{D} \cong 0 \tag{15}$$

As inferred from Eq. (15), the viability of applying fractal geometry to a porous medium pivot on the condition $\lambda_{\mathrm{max}} \gg \lambda_{\mathrm{min}}$. Typically, in porous media (and carbon foams), it is observed that $\lambda_{\mathrm{min}}/\lambda_{\mathrm{max}} <$

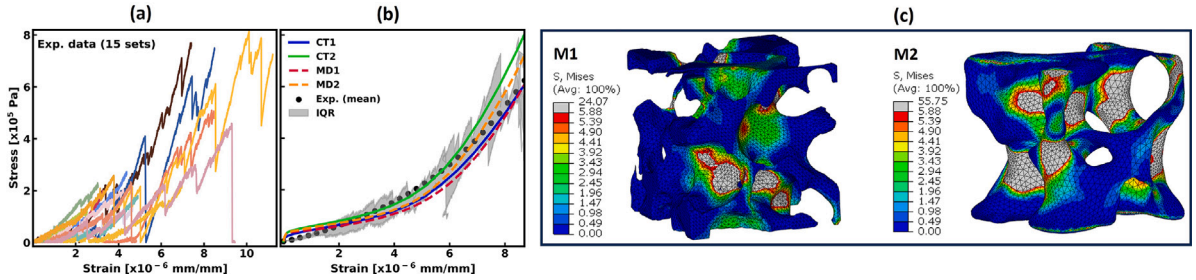

Fig. 8. (a) Experimental stress–strain plots of 15 dogbone samples. (b) The smoothed average of experimental tensile data and FEA tensile data for CT1, CT2, MD1, and MD2. The interquartile range (IQR), represented by the gray overlay, is the difference between the third (Q_3) and first (Q_1) quartiles. (c) Stress distribution in MD models M1 and M2.

10^{-2} [29,31,80–82], thus validating the applicability of fractal properties in such contexts.

Given the key role of pore characterization in validating our atomistic-to-continuum modeling approach, we present a detailed discussion of our implementation to obtain pore properties of the models using Avizo® in Section S2 of the supplementary material. Furthermore, we offer an explanatory video of this procedure utilizing the MD1 model, available as supplementary material, and on our website [63]. We aim to provide clear and comprehensive instructions to ensure replicability and facilitate the expansion of our methodology to other porous media.

3.3. Tortuosity analysis

Tortuosity is a morphological feature that describes the limiting influence of pore structure on the transport properties of porous materials. it represents the complexity of pore connectivity (e.g. sinuosity) in these materials and influences their electrical, thermal, and mechanical properties [83–85]. It is worth noting that tortuosity measurements should ideally be consistent. Still, discrepancies may arise due to the property studied, measurement techniques (i.e. geometric, hydraulic, conductive, diffusive...), and the material structure model [85,86]. Thus, interpreting tortuosity relies heavily on the chosen methodology, including 3D imaging, simulation, or laboratory experiments. In this work, hydraulic tortuosity (τ) for the MD and CT models was computed utilizing the following formula:

$$\tau = \sum_{i=0}^{n} \frac{\|\mathbf{v_i}\|}{\mathbf{v} \cdot z_i} \tag{16}$$

Here, n denotes the number of throats in the network, $\mathbf{v_i}$ represents the fluid velocity passing through the ith throat, and $\mathbf{v} \cdot z_i$ signifies the velocity projection along the flow direction (designated as z) through the ith throat. The velocities were derived from the absolute permeability obtained using the pore network model developed by Laroche and Vizika [87] for two-phase flow, albeit implemented here for a single phase, assuming the network is filled. The permeability computations were performed using Avizo®, and additional methodological details can be found in Ref. [88]. As shown in Table 1, the hydraulic tortuosity obtained for MD1, MD2, and MD3 are 1.49, 1.44, and 1.62, respectively, and 1.65, 1.50, and 1.50 for CT1, CT2, and CT3, respectively. The tortuosity values obtained for all the models are close and within the range obtained experimentally for carbon foam materials [85,89].

3.4. Tensile and deformation behavior

[90,91]. The stress–strain plots obtained for the 15 dogbone carbon foam samples are illustrated in Fig. 8a. Due to the brittle nature of carbon foam, variations in its mechanical properties are expected and have been well-documented in the literature [90,91]. The early failure observed in Fig. 8a can be attributed to defects or large pores in the specimen. For comparison with FEA tensile data, we computed the average stress and strain in the elastic region of the experimental dataset, excluding data points at and after failure. Fig. 8b illustrates the (smoothed) average stress for the 15 experimental datasets and the computed stress–strain curves for CT1, CT2, MD1, and MD2. CT3 and MD3 were intentionally left out since this study intends to explore model construction with fewer nodes and elements that can be processed in a modest workstation. Additionally, MD3 serves to show that bulk representation is also achievable using our method.

Given the variation in failure strain among specimens, alongside the mean stress–strain curve, we present the interquartile range (IQR) as a gray overlay, representing the difference between the upper and lower quartiles (Q_3 - Q_1). The IQR is a measure of data dispersion, crucial for identifying outliers that could distort traditional metrics such as range or standard deviation. The mean experimental and FEA strain-strain curves fall within the plotted IQR for the 15 datasets, confirming the absence of significant outliers.

The mean experimental stress–strain curve closely aligns with the behavior observed in both CT and MD models, albeit with a minor deviation where CT2 and MD2 exhibit slightly higher stiffness. This discrepancy arises from variations in the structural attributes of the models' struts. Specifically, the orientation of the struts in CT2 and MD2, parallel to the loading direction, enhances stiffness. A limitation of our method, as well as CT-scan-based modeling, lies in the inability to predetermine strut orientation. To address this, we propose generating ensembles of MD models and selecting optimal orientations—a computationally efficient alternative to constructing multiple CT models. Furthermore, our analysis suggests that stiffness is largely unaffected by foam porosity, as evidenced by similar porosity levels across all models (Table 1).

Fig. 8c illustrates the stress distribution on MD models, MD1 and MD2. Stress tends to accumulate at locations with abrupt geometry changes and in regions featuring thinner struts. Conversely, areas with closely interconnected struts exhibit more uniform stress distribution, often approaching zero. In contrast, less dense regions or isolated struts experience higher stress concentrations. These localized stress variations are crucial for evaluating overall structural integrity and identifying potential failure zones.

Understanding the deformation (failure) behavior of carbon foam, particularly its brittle tensile response, is crucial for elucidating its mechanical properties. Fig. 9 illustrates the simulated deformation response of the MD2 model, with an accompanying animation detailing the timeline of the brittle tensile response available as supplementary material, and on our website [63]. We reiterate that the damage cutoff stress was set to 5.88 MPa, which is the strength value in Table 1, determined based on the failure analysis of a single-element model. During the stages of brittle tensile response, rapid deformation and failure of the model were observed with minimal plasticity, as depicted in the middle panel of Fig. 9 (and the supplementary animation). This behavior aligns with experimental observations of carbon foam deformation, typically due to inherent defects such as voids, pores, and structural irregularities within the foam matrix, serving as initiation points for crack formation and propagation [90]. Further investigations into the factors influencing deformation, including foam density, pore

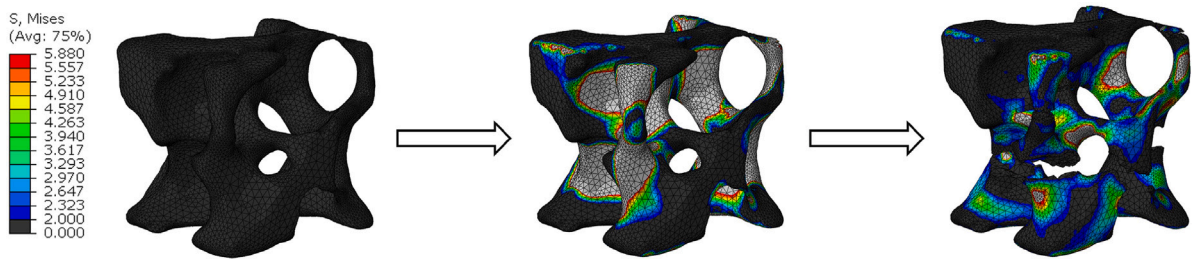

Fig. 9. The process of brittle tensile failure for the MD2 model is depicted. An animation showcasing the progression of the failure is provided as supplementary material, and also on our website [63].

structure, and the presence of additives, are reserved for future studies utilizing the MD models constructed herein. Thus, we present only preliminary findings on the deformation behavior of the MD models.

4. Conclusions

We integrated the precision of molecular dynamics simulation with the scalability and temporal efficiency of continuum modeling to develop models capable of accurately representing carbon foams, crucial for finite element analyses. Beginning with atomistic structures delineating a porous carbon network, the methodology involves a series of steps encompassing surface reconstruction and solid mesh processing to yield models suitable for finite element simulation. The justification for transitioning from atomistic to continuum models hinges on the inherent statistical similarity observed in porous media, including carbon foam, permitting the application of fractal geometries and properties to carbon foam. The comparison between the 2D Minkowski (box-counting) dimension and the 3D pore fractal dimension, based on a porosity power law relation, indicates comparable results for the two discussed models in this study. We showed that, despite variation between the length scales of the MD models and the CT model, the values obtained for the pore fractal dimension, as well as the ratio of the pore size to bounding box size, remain consistent across models. This further supports the statistical self-similarity of carbon foams.

To validate the MD models, 15 dogbone samples of coal-derived carbon foam (CFOAM®, sourced from CONSOL Innovations, WV, USA) were fabricated, and 3D models were obtained from computed tomography (CT) scanning of the CFOAM®. Tensile tests were conducted and the stress–strain curve obtained from averaging of the experimental dataset was shown to closely align with the FEA-calculated stress–strain curve for the MD models. Lastly, the deformation (or tensile brittle) response was discussed. This study presents a computationally efficient and statistically robust approach for deriving the desired macroscopic properties of carbon foam through finite element simulations.

We curated a set of supplementary materials to enhance the reproducibility and refinement of our methodology. An overview of what is included follows:

1. A traditional supplementary material document (PDF file) offering explanations for key discussions in this study.
2. A Web-App, *Porous Carbon Constructor*, that generates initial models of porous carbon before MD simulation [51].
3. A tutorial video showing how we compute pore properties in `Avizo®`.
4. All six configuration files of the FEA solid models featured in this study, provided in *.stl* format. We provided two extra CT models as well.
5. The `Mathematica` script used in computing the 3D box-counting dimensions of the models.
6. An animation illustrating the evolution of pores and the cross-linking of carbon atoms on pore surfaces during MD simulation to generate the MD porous carbon models.
7. An animation showcasing the brittle tensile response for the MD1 model.

Finally, we note that a promising application of our methodology is in examining high-temperature thermal conduction in carbon foams, where in-situ measurement methods are currently lacking [92]. Current simulation approaches via FEA [5,8,31,93] consider macro-porosity due to radiation propagation but overlook atomistic contributions from carbon–carbon interactions. Our method addresses this gap by developing integrated atomistic and continuum models for specific carbon foams. This allows for the simultaneous examination of carbon network instability, carbon–carbon vibrations (using atomistic representations and vibrational modes), and radiative contributions (using constructed FEA models). This dual modeling strategy provides a comprehensive understanding of the behavior and stability of carbon foams at high temperatures, offering valuable insights for both research and industrial applications.

CRediT authorship contribution statement

C. Ugwumadu: Writing – review & editing, Writing – original draft, Visualization, Validation, Supervision, Software, Resources, Project administration, Methodology, Investigation, Funding acquisition, Formal analysis, Data curation, Conceptualization. **W. Downs:** Writing – review & editing, Writing – original draft, Visualization, Validation, Software, Methodology, Investigation, Formal analysis, Data curation, Conceptualization. **C. O'Brien:** Writing – review & editing, Visualization, Methodology, Formal analysis. **R. Thapa:** Writing – review & editing, Software, Methodology, Investigation, Formal analysis, Conceptualization. **R. Olson III:** Writing – review & editing, Validation, Resources, Project administration, Investigation, Funding acquisition, Formal analysis, Data curation. **B. Wisner:** Validation, Writing – review & editing. **M. Ali:** Writing – review & editing, Supervision, Resources, Project administration, Methodology. **J. Trembly:** Writing – review & editing, Supervision, Resources, Project administration, Methodology, Funding acquisition. **Y. Al-Majali:** Writing – review & editing, Validation, Supervision, Resources, Project administration, Methodology, Funding acquisition. **D.A. Drabold:** Writing – review & editing, Validation, Supervision, Resources, Project administration, Methodology, Funding acquisition, Formal analysis, Conceptualization.

Declaration of competing interest

The authors declare that they have no known competing financial interests or personal relationships that could have appeared to influence the work reported in this paper.

Data availability

The data supporting the present study are publicly available on Zenodo (DOI: 10.5281/zenodo.10809805), and on the official website of the Materials Theory Group, Ohio University (MTG-OhioU) at https://people.ohio.edu/drabold/carbonfoam/.

Acknowledgments

C.U. expresses his appreciation to the Nanoscale & Quantum Phenomena Institute (NQPI) for the financial support conferred through the NQPI research fellowship. C. U. acknowledges Rawan Nowier for assistance editing the explainer video for the pore analysis. The authors thank Anna-Theresa Kirchtag for proofreading the manuscript.

Funding

C. U and D. A. D used computational resources at the Pittsburgh Supercomputing Center (Bridges-2 Regular Memory) through allocation phy230007p and dmr190008p from the Advanced Cyberinfrastructure Coordination Ecosystem: Services & Support (ACCESS) programs, supported by the National Science Foundation (NSF), USA grants: 2138259, 2138286, 2138307, 2137603, and 2138296.

Appendix A. Supplementary data

Supplementary material related to this article can be found online at https://doi.org/10.1016/j.carbon.2024.119506.

References

[1] D. Haack, R. Olson III, Processing, microstructure and properties of reticulated vitreous carbon foam manufactured via the sponge replication technique, in: Advances in Bioceramics and Porous Ceramics V, John Wiley & Sons, Ltd, 2012, pp. 175–185, http://dx.doi.org/10.1002/9781118217504.ch20, (Chapter II).

[2] M. Inagaki, J. Qiu, Q. Guo, Carbon foam: Preparation and application, Carbon 87 (2015) 128–152, http://dx.doi.org/10.1016/j.carbon.2015.02.021.

[3] A. Fehér, R. Kovács, Á. Sudár, G.G. Barnaföldi, Challenges in the thermal modeling of highly porous carbon foams, J. Therm. Anal. Calorim. (2024) 1–12, http://dx.doi.org/10.1007/s10973-024-12927-w.

[4] N. Bogumiła, P. Sławomira, B. Trzebicka, Tailoring the properties of macroporous carbon foams, J. Mater. Sci. 49 (1) (2014) 1–17, http://dx.doi.org/10.1007/s10853-013-7678-x.

[5] A.M. Druma, M.K. Alam, C. Druma, Analysis of thermal conduction in carbon foams, Int. J. Therm. Sci. 43 (7) (2004) 689–695, http://dx.doi.org/10.1016/j.ijthermalsci.2003.12.004.

[6] Q. Yu, B.E. Thompson, A.G. Straatman, A unit cube-based model for heat transfer and fluid flow in porous carbon foam, J. Heat Transfer 128 (4) (2005) 352–360, http://dx.doi.org/10.1115/1.2165203.

[7] K. Leong, H. Li, Theoretical study of the effective thermal conductivity of graphite foam based on a unit cell model, Int. J. Heat Mass Transfer 54 (25–26) (2011) 5491–5496, http://dx.doi.org/10.1016/j.ijheatmasstransfer.2011.07.042.

[8] Y. Chai, X. Yang, M. Zhao, Z. Chen, X. Meng, L. Jin, Q. Zhang, W. Hu, Study of microstructure-based effective thermal conductivity of graphite foam, J. Heat Transfer 139 (5) (2017) 052004, http://dx.doi.org/10.1115/1.4036002.

[9] A. Roberts, E. Garboczi, Elastic moduli of model random three-dimensional closed-cell cellular solids, Acta Mater. 49 (2) (2001) 189–197, http://dx.doi.org/10.1016/S1359-6454(00)00314-1.

[10] A. Roberts, E. Garboczi, Elastic properties of model random three-dimensional open-cell solids, J. Mech. Phys. Solids 50 (1) (2002) 33–55, http://dx.doi.org/10.1016/S0022-5096(01)00056-4.

[11] Y. Song, Z. Wang, L. Zhao, J. Luo, Dynamic crushing behavior of 3D closed-cell foams based on voronoi random model, Mater. Des. 31 (9) (2010) 4281–4289, http://dx.doi.org/10.1016/j.matdes.2010.04.007.

[12] M. Kırca, A. Gül, E. Ekinci, F. Yardım, A. Mugan, Computational modeling of micro-cellular carbon foams, Finite Elem. Anal. Des. 44 (1–2) (2007) 45–52, http://dx.doi.org/10.1016/j.finel.2007.08.008.

[13] L. James, S. Austin, C.A. Moore, D. Stephens, K.K. Walsh, G.D. Wesson, Modeling the principle physical parameters of graphite carbon foam, Carbon 48 (9) (2010) 2418–2424, http://dx.doi.org/10.1016/j.carbon.2010.02.043.

[14] P. Yue, X. Li, X. Guo, Y. Cheng, K. Li, X. Cheng, Stochastic microstructure modeling and thermal conductivity of coal-based carbon foam, Mater. Today Commun. 39 (2024) 108994, http://dx.doi.org/10.1016/j.mtcomm.2024.108994.

[15] W. Moddeman, D. Kramer, D. Firsich, P. Trainer, R. Yancy, D. Weirup, C. Logan, A. Pontau, A. Antolak, D. Morse, Characterization of low density carbon foams by X-ray computed tomography (CT) and ion microtomography (IMT), MRS Online Proc. Libr. (OPL) 217 (1990) 205, http://dx.doi.org/10.1557/PROC-217-205.

[16] F. Arand, J. Hesser, Quantitative morphological analysis and digital modeling of polydisperse anisotropic carbon foam, Carbon 136 (2018) 11–20, http://dx.doi.org/10.1016/j.carbon.2018.04.049.

[17] I. Jeon, T. Asahina, K.-J. Kang, S. Im, T.J. Lu, Finite element simulation of the plastic collapse of closed-cell aluminum foams with X-ray computed tomography, Mech. Mater. 42 (3) (2010) 227–236, http://dx.doi.org/10.1016/j.mechmat.2010.01.003.

[18] C. Ugwumadu, R. Thapa, K. Nepal, A. Gautam, Y. Al-Majali, J. Trembly, D.A. Drabold, Self-assembly and the properties of micro-mesoporous carbon, J. Chem. Theory Comput. (2023) http://dx.doi.org/10.1021/acs.jctc.3c00394.

[19] R. Rudd, J. Broughton, Concurrent coupling of length scales in solid state systems, Phys. Status Solidi (B) 217 (1) (2000) 251–291, http://dx.doi.org/10.1002/(SICI)1521-3951(200001)217:1<251::AID-PSSB251>3.0.CO;2-A.

[20] L. Shilkrot, W.A. Curtin, R.E. Miller, A coupled atomistic/continuum model of defects in solids, J. Mech. Phys. Solids 50 (10) (2002) 2085–2106, http://dx.doi.org/10.1016/S0022-5096(02)00017-0.

[21] V. Shenoy, R. Miller, E. Tadmor, R. Phillips, M. Ortiz, Quasicontinuum models of interfacial structure and deformation, Phys. Rev. Lett. 80 (4) (1998) 742, http://dx.doi.org/10.1103/PhysRevLett.80.742.

[22] H. Wu, G. Liu, X. Han, X. Wang, An atomistic simulation method combining molecular dynamics with finite element technique, Chaos Solitons Fractals 30 (4) (2006) 791–796, http://dx.doi.org/10.1016/j.chaos.2005.08.161.

[23] C.R. Weinberger, G.J. Tucker (Eds.), Multiscale Materials Modeling for Nanomechanics, Springer, Cham, 2016, http://dx.doi.org/10.1007/978-3-319-33480-6.

[24] M. Ortiz, A. Cuitino, J. Knap, M. Koslowski, Mixed atomistic–continuum models of material behavior: The art of transcending atomistics and informing continua, MRS Bull. 26 (3) (2001) 216–221, http://dx.doi.org/10.1557/mrs2001.45.

[25] T.M. Ajayi, N. Shirato, T. Rojas, S. Wieghold, X. Cheng, K.Z. Latt, D.J. Trainer, N.K. Dandu, Y. Li, S. Premarathna, et al., Characterization of just one atom using synchrotron X-rays, Nature 618 (7963) (2023) 69–73, http://dx.doi.org/10.1038/s41586-023-06011-w.

[26] B.B. Mandelbrot, B.B. Mandelbrot, The fractal geometry of nature, vol. 1, WH Freeman, New York, 1982.

[27] S. Graf, Statistically self-similar fractals, Probab. Theory Related Fields 74 (3) (1987) 357–392, http://dx.doi.org/10.1007/BF00699096.

[28] A.J. Katz, A.H. Thompson, Fractal sandstone pores: Implications for conductivity and pore formation, Phys. Rev. Lett. 54 (1985) 1325–1328, http://dx.doi.org/10.1103/PhysRevLett.54.1325.

[29] B. Yu, J. Li, Some fractal characters of porous media, Fractals 9 (03) (2001) 365–372, http://dx.doi.org/10.1142/S0218348X01000804.

[30] B. Yu, P. Cheng, A fractal permeability model for bi-dispersed porous media, Int. J. Heat Mass Transfer 45 (14) (2002) 2983–2993, http://dx.doi.org/10.1016/S0017-9310(02)00014-5.

[31] T. Xiao, X. Yang, K. Hooman, L. Jin, C. Yang, T.J. Lu, Conductivity and permeability of graphite foams: Analytical modelling and pore-scale simulation, Int. J. Therm. Sci. 179 (2022) 107706, http://dx.doi.org/10.1016/j.ijthermalsci.2022.107706.

[32] P. Hohenberg, W. Kohn, Inhomogeneous electron gas, Phys. Rev. 136 (1964) B864–B871, http://dx.doi.org/10.1103/PhysRev.136.B864.

[33] R. Thapa, D.A. Drabold, *Ab Initio* simulation of amorphous materials, in: Atomistic Simulations of Glasses, John Wiley & Sons, Ltd, 2022, pp. 30–59, http://dx.doi.org/10.1002/9781118939079.ch2, (Chapter 2).

[34] V. Botu, R. Batra, J. Chapman, R. Ramprasad, Machine learning force fields: Construction, validation, and outlook, J. Phys. Chem. C 121 (1) (2017) 511–522, http://dx.doi.org/10.1021/acs.jpcc.6b10908.

[35] V.L. Deringer, N. Bernstein, G. Csányi, M. Wilson, D.A. Drabold, S.R. Elliott, Structural transitions in dense disordered silicon from quantum-accurate ultra-large-scale simulations, Nature (2021) http://dx.doi.org/10.1038/s41586-020-03072-z.

[36] C. van der Oord, M. Sachs, D.P. Kovács, C. Ortner, G. Csányi, Hyperactive learning for data-driven interatomic potentials, NPJ Comput. Mater. 9 (1) (2023) 168, http://dx.doi.org/10.1038/s41524-023-01104-6.

[37] J.D. Morrow, V.L. Deringer, Indirect learning and physically guided validation of interatomic potential models, J. Chem. Phys. 157 (10) (2022) http://dx.doi.org/10.1063/5.0099929.

[38] J.D. Morrow, C. Ugwumadu, D.A. Drabold, S.R. Elliott, A.L. Goodwin, V.L. Deringer, Understanding defects in amorphous silicon with million-atom simulations and machine learning, Angew. Chem. Int. Ed. 63 (22) (2024) e202403842, http://dx.doi.org/10.1002/anie.202403842.

[39] S. Klawohn, J.P. Darby, J.R. Kermode, G. Csányi, M.A. Caro, A.P. Bartók, Gaussian approximation potentials: Theory, software implementation and application examples, J. Chem. Phys. 159 (17) (2023) 174108, http://dx.doi.org/10.1063/5.0160898.

[40] V.L. Deringer, G. Csányi, Machine learning based interatomic potential for amorphous carbon, Phys. Rev. B 95 (2017) 094203, http://dx.doi.org/10.1103/PhysRevB.95.094203.

[41] V.L. Deringer, A.P. Bartók, N. Bernstein, D.M. Wilkins, M. Ceriotti, G. Csányi, Gaussian process regression for materials and molecules, Chem. Rev. 121 (16) (2021) 10073–10141, http://dx.doi.org/10.1021/acs.chemrev.1c00022.

[42] M.A. Caro, G. Csányi, T. Laurila, V.L. Deringer, Machine learning driven simulated deposition of carbon films: From low-density to diamondlike amorphous carbon, Phys. Rev. B 102 (2020) 174201, http://dx.doi.org/10.1103/PhysRevB.102.174201.

[43] V.L. Deringer, M.A. Caro, R. Jana, A. Aarva, S.R. Elliott, T. Laurila, G. Csányi, L. Pastewka, Computational surface chemistry of tetrahedral amorphous carbon by combining machine learning and density functional theory, Chem. Mater. 30 (21) (2018) 7438–7445, http://dx.doi.org/10.1021/acs.chemmater.8b02410.

[44] S. Fujikake, V.L. Deringer, T.H. Lee, M. Krynski, S.R. Elliott, G. Csányi, Gaussian approximation potential modeling of lithium intercalation in carbon nanostructures, J. Chem. Phys. 148 (24) (2018) 241714, http://dx.doi.org/10.1063/1.5016317.

[45] A.P. Thompson, H.M. Aktulga, R. Berger, D.S. Bolintineanu, W.M. Brown, P.S. Crozier, P.J. in 't Veld, A. Kohlmeyer, S.G. Moore, T.D. Nguyen, R. Shan, M.J. Stevens, J. Tranchida, C. Trott, S.J. Plimpton, LAMMPS - a flexible simulation tool for particle-based materials modeling at the atomic, meso, and continuum scales, Comput. Phys. Comm. 271 (2022) 108171, http://dx.doi.org/10.1016/j.cpc.2021.108171.

[46] R. Thapa, C. Ugwumadu, K. Nepal, J. Trembly, D.A. Drabold, Ab initio simulation of amorphous graphite, Phys. Rev. Lett. 128 (2022) 236402, http://dx.doi.org/10.1103/PhysRevLett.128.236402.

[47] C. Ugwumadu, R. Thapa, K. Nepal, D.A. Drabold, Atomistic nature of amorphous graphite, Eur. J. Glass Sci. Technol. B 64 (2023) 16–22, http://dx.doi.org/10.13036/17533562.64.1.18.

[48] C. Ugwumadu, K. Nepal, R. Thapa, Y. Lee, Y. Al Majali, J. Trembly, D. Drabold, Simulation of multi-shell fullerenes using machine-learning Gaussian approximation potential, Carbon Trends 10 (2023) 100239, http://dx.doi.org/10.1016/j.cartre.2022.100239.

[49] C. Ugwumadu, R. Thapa, Y. Al-Majali, J. Trembly, D.A. Drabold, Formation of amorphous carbon multi-walled nanotubes from random initial configurations, Phys. Status Solidi (B) 260 (3) (2023) 2200527, http://dx.doi.org/10.1002/pssb.202200527.

[50] Streamlit, Streamlit: A faster way to build and share data apps, 2024, URL https://streamlit.io/.

[51] C. Ugwumadu, D. Drabold, Porous carbon constructor app, available on the materials theory group-Ohio university (MTG-OhioU) app center, 2024, URL https://mtg-ohiou.streamlit.app/Porous_Carbon.

[52] M.P. Allen, D.J. Tildesley, Computer simulation of liquids, second ed., Clarendon Press, Oxford, 2017, pp. 1–34, (Chapter 1).

[53] H. Edelsbrunner, E.P. Mücke, Three-dimensional alpha shapes, in: Proceedings of the 1992 Workshop on Volume Visualization, VVS '92, Association for Computing Machinery, New York, NY, USA, 1992, pp. 75–82, http://dx.doi.org/10.1145/147130.147153.

[54] B. Delaunay, et al., Sur la sphere vide, Izv. Akad. Nauk SSSR Otd. Mat. Estestvennyka Nauk 7 (793–800) (1934) 1–2.

[55] A. Stukowski, Computational analysis methods in atomistic modeling of crystals, JOM 66 (3) (2014) 399–407, http://dx.doi.org/10.1007/s11837-013-0827-5.

[56] S. Nosé, A molecular dynamics method for simulations in the canonical ensemble, Mol. Phys. 52 (2) (1984) 255–268, http://dx.doi.org/10.1080/00268978400101201.

[57] W.G. Hoover, Canonical dynamics: Equilibrium phase-space distributions, Phys. Rev. A 31 (1985) 1695–1697, http://dx.doi.org/10.1103/PhysRevA.31.1695.

[58] M.D. Artimez, New Method of Manufacturing Carbon Foam (Master's thesis), West Virginia University, 2019, http://dx.doi.org/10.33915/etd.4039.

[59] A. Stukowski, Visualization and analysis of atomistic simulation data with OVITO–the open visualization tool, Modelling Simul. Mater. Sci. Eng. 18 (1) (2009) 015012, http://dx.doi.org/10.1088/0965-0393/18/1/015012.

[60] G. Taubin, A signal processing approach to fair surface design, in: Proceedings of the 22nd Annual Conference on Computer Graphics and Interactive Techniques, Association for Computing Machinery, New York, NY, USA, 1995, pp. 351–358, http://dx.doi.org/10.1145/218380.218473.

[61] W. Schroeder, K. Martin, B. Lorensen, The Visualization Toolkit, fourth ed., Kitware, 2006.

[62] G.G. Jacob, C.C. Kai, T. Mei, Development of a new rapid prototyping interface, Comput. Ind. 39 (1) (1999) 61–70, http://dx.doi.org/10.1016/S0166-3615(98)00124-9.

[63] Materials Theory Group, Ohio University, Athens OH, USA, Website containing the supplementary materials for the present study, 2024, URL https://people.ohio.edu/drabold/carbonfoam/. (Accessed 20 April 2024).

[64] J.P. Ahrens, B. Geveci, C.C. Law, ParaView: An end-user tool for large-data visualization, in: C.D. Hansen, C.R. Johnson (Eds.), Visualization Handbook, Butterworth-Heinemann, Burlington, 2005, pp. 717–731, http://dx.doi.org/10.1016/B978-012387582-2/50038-1.

[65] U. Ayachit, The ParaView Guide: A Parallel Visualization Application, Kitware, Inc., Clifton Park, NY, USA, 2015.

[66] O. Muller-Girard, Instruments: Measurement of linear and angular displacement, in: Standard Handbook for Mechanical Engineers, tenth ed., McGraw-Hill, 1996, pp. 5–6, (Chapter 16).

[67] K. Li, X.-L. Gao, A. Roy, Micromechanics model for three-dimensional open-cell foams using a tetrakaidecahedral unit cell and Castigliano's second theorem, Compos. Sci. Technol. 63 (12) (2003) 1769–1781, http://dx.doi.org/10.1016/S0266-3538(03)00117-9.

[68] M. Kırca, A. Gül, E. Ekinci, F.Y. m, A. Mugan, Computational modeling of micro-cellular carbon foams, Finite Elem. Anal. Des. 44 (1) (2007) 45–52, http://dx.doi.org/10.1016/j.finel.2007.08.008.

[69] Psylotech, *mu*TS user manual V2.09 may 2022, 2024, URL https://psylotech.com/wp-content/uploads/2023/01/%C2%B5TS_Users_Manual_2.09-GRIPS-ONLY.pdf. Geometry specification for testing samples.

[70] R.E. Jones, J. Templeton, J. Zimmerman, Principles of coarse-graining and coupling using the atom-to-continuum method, in: Multiscale Materials Modeling for Nanomechanics, Springer, Cham, 2016, pp. 223–259, http://dx.doi.org/10.1007/978-3-319-33480-6_7, (Chapter 1).

[71] M.F. Ashby, L.J. Gibson, Cellular Solids: Structure and Properties, Press Syndicate of the University of Cambridge, Cambridge, UK, 1997, p. 218, (Chapter 5).

[72] W.E. Warren, A.M. Kraynik, The nonlinear elastic behavior of open-cell foams, J. Appl. Mech. 58 (2) (1991) 376–381, http://dx.doi.org/10.1115/1.2897196.

[73] A. Eksilioglu, N. Gencay, M.F. Yardim, E. Ekinci, Mesophase AR pitch derived carbon foam: Effect of temperature, pressure and pressure release time, J. Mater. Sci. 41 (2006) 2743–2748, http://dx.doi.org/10.1007/s10853-006-7079-5.

[74] P. Grassberger, On the fractal dimension of the Henon attractor, Phys. Lett. A 97 (6) (1983) 224–226, http://dx.doi.org/10.1016/0375-9601(83)90752-1.

[75] L.S. Liebovitch, T. Toth, A fast algorithm to determine fractal dimensions by box counting, Phys. Lett. A 141 (8) (1989) 386–390, http://dx.doi.org/10.1016/0375-9601(89)90854-2.

[76] J.T. Gostick, Z.A. Khan, T.G. Tranter, M.D. Kok, M. Agnaou, M. Sadeghi, R. Jervis, PoreSpy: A python toolkit for quantitative analysis of porous media images, J. Open Source Softw. 4 (37) (2019) 1296, http://dx.doi.org/10.21105/joss.01296.

[77] W.R. Inc., Mathematica, version 14.0, 2024, URL https://www.wolfram.com/mathematica. Champaign, IL, 2024.

[78] A. Majumdar, B. Bhushan, Role of fractal geometry in roughness characterization and contact mechanics of surfaces, J. Tribol. Trans. ASME 112 (1990) 205–216, http://dx.doi.org/10.1115/1.2920243.

[79] T. Vicsek, Fractal Growth Phenomena, second ed., World Scientific, 1992, http://dx.doi.org/10.1142/1407.

[80] M. Inagaki, Pores in carbon materials-importance of their control, New Carbon Mater. 24 (3) (2009) 193–232, http://dx.doi.org/10.1016/S1872-5805(08)60048-7.

[81] S. Li, X. Tan, H. Li, Y. Gao, Q. Wang, G. Li, M. Guo, Investigation on pore structure regulation of activated carbon derived from sargassum and its application in supercapacitor, Sci. Rep. 12 (1) (2022) 10106, http://dx.doi.org/10.1038/s41598-022-14214-w.

[82] S.M. Manocha, Porous carbons, Sadhana 28 (2003) 335–348, http://dx.doi.org/10.1007/BF02717142.

[83] B.J. Christensen, T. Coverdale, R.A. Olson, S.J. Ford, E.J. Garboczi, H.M. Jennings, T.O. Mason, Impedance spectroscopy of hydrating cement-based materials: measurement, interpretation, and application, J. Am. Ceram. Soc. 77 (11) (1994) 2789–2804, http://dx.doi.org/10.1111/j.1151-2916.1994.tb04507.x.

[84] L. Holzer, P. Marmet, M. Fingerle, A. Wiegmann, M. Neumann, V. Schmidt, Review of theories and a new classification of tortuosity types, in: Tortuosity and Microstructure Effects in Porous Media: Classical Theories, Empirical Data and Modern Methods, Springer International Publishing, Cham, 2023, pp. 7–50, http://dx.doi.org/10.1007/978-3-031-30477-4_2, (Chapter 2).

[85] M. Letellier, V. Fierro, A. Pizzi, A. Celzard, Tortuosity studies of cellular vitreous carbon foams, Carbon 80 (2014) 193–202, http://dx.doi.org/10.1016/j.carbon.2014.08.056.

[86] M.B. Clennell, Tortuosity: a guide through the maze, Geol. Soc. Lond. Spec. Publ. 122 (1) (1997) 299–344, http://dx.doi.org/10.1144/GSL.SP.1997.122.01.18.

[87] C. Laroche, O. Vizika, Two-phase flow properties prediction from small-scale data using pore-network modeling, Transp. Porous Media 61 (2005) 77–91, http://dx.doi.org/10.1007/s11242-004-6797-x.

[88] S. Youssef, E. Rosenberg, N. Gland, J.A.M. Kenter, M. Skalinski, O. Vizika, High resolution CT and pore-network models to assess petrophysical properties of homogeneous and heterogeneous carbonates, in: SPE Reservoir Characterisation and Simulation Conference and Exhibition, 2007, pp. SPE–111427–MS, http://dx.doi.org/10.2118/111427-MS.

[89] T. Gómez Álvarez-Arenas, S. De la Fuente, I. González Gómez, Simultaneous determination of apparent tortuosity and microstructure length scale and shape: Application to rigid open cell foams, Appl. Phys. Lett. 88 (22) (2006) 221910, http://dx.doi.org/10.1063/1.2208921.

[90] Z. Li, W. Chen, H. Hao, Mechanical properties of carbon foams under quasi-static and dynamic loading, Int. J. Mech. Sci. 161–162 (2019) 105039, http://dx.doi.org/10.1016/j.ijmecsci.2019.105039.

[91] S. Gowthaman, K. Shivakumar, P. Mathiyalagan, End-potting concept for compression testing of open-cell carbon foams, Exp. Tech. 40 (2016) 357–366, http://dx.doi.org/10.1007/s40799-016-0039-3.

[92] Thermset™Instruments, Laser flash method, 2024, URL https://thermtest.com/history-3-laser-flash-method. (Accessed 6 June 2024).

[93] J. Klett, R. Hardy, E. Romine, C. Walls, T. Burchell, High-thermal-conductivity, mesophase-pitch-derived carbon foams: effect of precursor on structure and properties, Carbon 38 (7) (2000) 953–973, http://dx.doi.org/10.1016/S0008-6223(99)00190-6.